Terahertz surface modes and electron-phonon coupling on $Bi_2Se_3(111)$

Adrian Ruckhofer [1,*] Davide Campi [2] Martin Bremholm [3] Philip Hofmann [4] Giorgio Benedek [5,6] Marco Bernasconi [5] Wolfgang E. Ernst [1] and Anton Tamtögl [1,†]

[1]*Institute of Experimental Physics, Graz University of Technology, Graz, Austria*
[2]*THEOS and MARVEL, École Polytechnique Fédérale de Lausanne, Lausanne, Switzerland*
[3]*Center for Materials Crystallography, Department of Chemistry and iNANO, Aarhus University, 8000 Aarhus, Denmark*
[4]*Department of Physics and Astronomy, Aarhus University, Aarhus, Denmark*
[5]*Dipartimento di Scienza dei Materiali, Università degli Studi di Milano-Bicocca, Milano, Italy*
[6]*Donostia International Physics Center (DIPC) and University of the Basque Country, 20018 Donostia / San Sebastian, Spain*

(Received 13 August 2019; accepted 13 April 2020; published 19 May 2020)

We present a combined experimental and theoretical study of the surface vibrational modes of the topological insulator Bi_2Se_3 with particular emphasis on the low-energy region below 10 meV that has been difficult to resolve experimentally. By applying inelastic helium atom scattering (HAS), the entire phonon dispersion was determined and compared with density functional perturbation theory (DFPT) calculations. The intensity of the phonon modes is dominated by a strong Rayleigh mode, in contrast to previous experimental works. Moreover, also at variance with recent reports, no Kohn anomaly is observed. These observations are in excellent agreement with DFPT calculations. Besides these results, the experimental data reveal—via bound-state resonance enhancement—two additional dispersion curves in the gap below the Rayleigh mode. They are possibly associated with an excitation of a surface electron density superstructure that we observe in HAS diffraction patterns. The electron-phonon coupling parameter $\lambda = 0.23$, derived from our temperature-dependent Debye-Waller measurements, compares well with values determined by angular resolved photoemission or Landau level spectroscopy. Our work opens up a new perspective for terahertz (THz) measurements on two-dimensional (2D) materials as well as the investigation of subtle details (band bending, the presence of a 2D electron gas) with respect to the electron-phonon coupling.

DOI: 10.1103/PhysRevResearch.2.023186

I. INTRODUCTION

Bi_2Se_3 (Fig. 1) is categorized as a three-dimensional topological insulator (TI), a new state of quantum matter with a bulk gap and spin-orbit split surface states forming a Dirac cone across the gap [1,2]. The interaction of electrons with surface phonons in Bi_2Se_3 has been studied intensively due to its important role in transport properties and possible constraints for potential applications in a variety of nanotechnologies [3–9]. Bismuth selenide as well as telluride alloys are classical thermoelectric materials [10,11] with a large Seebeck coefficient and, as such, they have been used in thermoelectric refrigeration for a long time [12]. However, to fully understand the thermoelectric properties of Bi_2Se_3 thin films and nanoscale devices [13,14], information on the surface phonon dispersion curves and the electron-phonon (e-ph) interaction is crucial [13,15,16].

So far experimental information about the surface phonon dispersion curves of $Bi_2Se_3(111)$ was limited to previous helium atom scattering (HAS) studies by Zhu *et al.* [7,17], in the low-energy part of the phonon spectrum. These studies suggested the presence of a deep Kohn anomaly (KA) in the 7.5 meV optical phonon branch (S2) coupled to the electronic (spin-forbidden) transition across the Dirac cone [17]. However, existing first-principle calculations of $Bi_2Se_3(111)$ phonon dispersion curves, do not show any evidence of KAs in the S2 branch [18].

A convenient parameter to characterize the e-ph coupling strength is the mass-enhancement λ [21] and in recent years it was demonstrated that HAS from conducting surfaces can directly measure the mode-selected e-ph coupling constants $\lambda_{\mathbf{Q},j}$ [22,23], besides the surface phonon dispersion curves [24]. Moreover the temperature-dependence of the HAS Debye-Waller factor was shown to provide the global e-ph coupling constant λ at the surface of thin metal films [24,25] and topological insulators [26,27]. Yet the large λ as estimated based on the KA [7] is at odds with theoretical findings that indicate that the major contribution to λ comes from the higher optical phonon branches [18], especially when the Fermi level crosses the surface quantum-well states above the conduction band minimum [see Fig. 1(c)]. The situation is actually met in recent high-resolution ^{3}He-spin scattering studies on $Bi_2Te_3(111)$, where the weak signature of a KA

*ruckhofer@tugraz.at
†tamtoegl@gmail.com

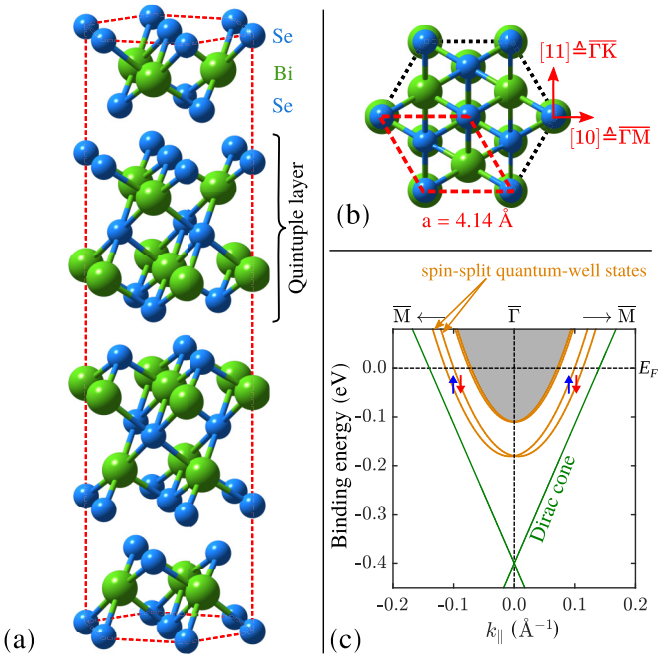

FIG. 1. (a) Crystal structure of Bi_2Se_3 based on the conventional hexagonal unit cell. The unit cell consists of three quintuple layers of which each one is terminated by a Se layer. (b) Top view of the (111) surface with the red rhombus illustrating the hexagonal surface unit cell with lattice constant a. The two high-symmetry scanning directions are indicated by the red arrows. (c) Illustration of the electronic dispersion around the $\overline{\Gamma}$ point (see Refs. [19,20]). Despite the Dirac cone, quantum-well states as illustrated by the orange lines exist on the surface as well. The quantum-well states are split due to Rashba coupling, thus making the previously degenerate spin states (illustrated by the red and blue arrows) separate into an inner and outer branch, each having a spin texture with opposite chirality.

is detected in the surface longitudinal acoustic resonance [28], also not found in adiabatic *ab initio* calculations of the phonon branches.

In order to elucidate these conflicting results, we have undertaken a HAS study of the surface phonon dispersion curves and the e-ph interaction of Bi_2Se_3(111). Supersonic neutral He atom beams with incident energies in the range $\leqslant$20 meV have been used to probe low-energy surface excitations with the best available resolution, while being an inert completely nondestructive probe [24,29]. The technique allows to measure most of the surface phonon branches in the acoustic and optical regions. Low-energy He atoms impinging on a conducting surface are exclusively scattered by the surface charge density [23,30] and inelastic scattering from surface phonons only occurs via the phonon-induced charge density oscillations, i.e., via the e-ph interaction. It is in this way that inelastic HAS provides a first-hand information on the e-ph interaction, with the neutral He atoms acting as a sort of local mechanical probe on the electron density.

Energy and momentum, inelastically exchanged by He atoms with the surface can, however, be retained by the electron system in the form of low-energy collective excitations. In principle, the HAS signal from this kind of excitations is expected to be quite small. Nevertheless, an increased e-ph interaction due to surface quantum-well states [31] in combination with an enhancement from HAS bound-state resonances [32], suggests to assign two branches of low-energy modes in the gap well below the Rayleigh waves (RW) to some sort of collective electronic excitations. Actually anomalous acoustic plasmons have been recently reported in Bi_2Se_3(111) by Jia *et al.* [33], from high-resolution electron energy-loss spectroscopy, although these modes turn out to be superimposed in the first Brillouin zone onto the RW branch.

Plasmons in a two-dimensional electron gas (2DEG) with a $\sqrt{Q}$ dispersion in dependence of a parallel wave vector Q (2D plasmons) have been predicted long ago by Frank Stern [34,35]. Later it was shown that the coupling of 2DEG plasmons arising from two different quantum-well minibands, as found in semiconductor surface accumulation layers, yields a surface plasmon pair: a 2D plasmon and an acoustic surface plasmon (ASP) with a linear dispersion above the upper edge of the single-particle excitation spectrum [36,37]. Similarly the coupling of a 2DEG at a metal surface coupled to the underlying 3D electron gas yields an ASP in addition to the ordinary surface plasmon [31,38–40]. As discussed below, the assignment of the two additional low-energy branches as collective polaron excitation recently suggested by Shvonski *et al.* [36], although plausible in semimetals with a large dielectric constant, definitely requires further *ad hoc* studies, possibly with even higher resolution as available, e.g., with ^{3}He spin-echo spectroscopy [28,41].

II. EXPERIMENTAL AND COMPUTATIONAL DETAILS

a. Experimental details. The reported measurements were performed on a HAS apparatus which generates a nearly monochromatic beam ($\Delta E/E \approx 2\%$) of ^{4}He that is scattered off the sample surface in a fixed 91.5° source-sample-detector geometry. The beam is produced in a supersonic expansion of He through a 10 μm nozzle followed by sampling the core of the supersonic expansion via a 310 μm skimmer. For a detailed description of the apparatus please refer to Ref. [42].

Energy dispersive measurements for inelastic scattering can be performed using time-of-flight (TOF) measurements with a pseudorandom chopper disk. After deconvolution with the pseudo random chopper sequence, the TOF signal is further transformed to an energy transfer scale which allows to determine inelastic (phonon) scattering events [42]. The scattering spectra were mainly taken with the crystal at room temperature, while a few spectra were taken with the sample cooled down to 115 K. The incident He beam energy was varied between 10 and 18 meV.

The crystal structure of Bi_2Se_3 is rhombohedral, formed of quintuple layers (QLs) which are bound to each other through weak van der Waals forces [43]. The hexagonal unit cell of the Bi_2Se_3 crystal, shown in Fig. 1, consists of three QLs. Each QL is terminated by Se atoms, giving rise to the (111) cleavage plane that exhibits a hexagonal structure [$a =$ 4.14 Å at room temperature [44], see Fig. 1(b)]. The Bi_2Se_3 crystal was attached onto a sample holder using thermally conductive epoxy. The sample holder was then inserted into the transfer chamber using a load-lock system and cleaved *in situ* [45]. The sample can be heated using a button heater on the backside of the crystal or cooled down to 115 K

via a thermal connection to a liquid nitrogen reservoir. The sample temperature was measured using a chromel-alumel thermocouple.

b. Computational details. The surface dynamical properties of Bi_2Se_3 were studied using density functional perturbation theory (DFPT) calculations [46] within the QUANTUM ESPRESSO package [47]. Norm-conserving pseudopotentials and the Perdew-Burke-Ernzerhof (PBE) approximation [48] for the exchange and correlation functional were used as implemented in the QUANTUM ESPRESSO package. The surface phonon dispersion was calculated using a slab consisting of 3 QLs separated from its periodic replica by 20 Å of vacuum, without the inclusion of spin-orbit corrections (SOC) (see also Appendix A for calculations with SOC). For an accurate calculation of the surface lattice vibrations, in principle, both SOC and van der Waals (vdW) corrections are necessary, both due to the presence of heavy elements in the compound and the latter to fully account for the weak bonds between the individual quintuple layers. However, as thoroughly discussed for Bi_2Te_3(111) [28], it appears that for layered crystals with heavy elements SOC alone gives a general softening of the phonon spectrum, compensated by the inclusion of vdW corrections, so that satisfactory results are obtained at a minor computational cost without both SOC and vdW corrections and with a better agreement with experiment [23,49]. Also for Bi_2Se_3 better agreement with the experiment is achieved with no SOC and no vdW corrections (see Sec. III A), likely due to a compensation of errors between the underbinding often characterising PBE functionals and SOC contributions and the overbinding due to vdW forces [28]. More precisely, the effect of SOC was found however to be weak for the low-energy surface vibrational modes of typical TIs such as Bi_2Te_3 and Sb_2Te_3 [28,50], while on the other hand, it was shown that vdW corrections become important for an exact description of the low-energy optical modes of Bi_2Te_3 [28].

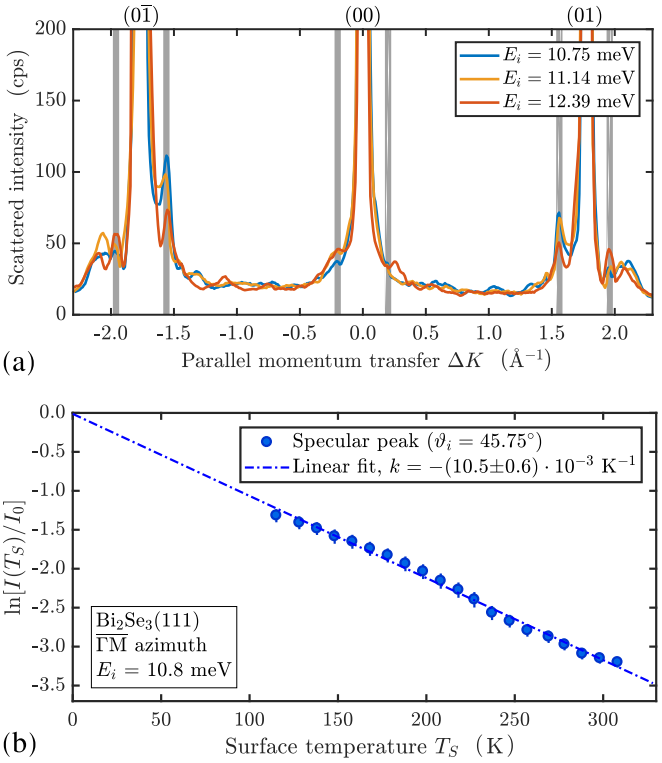

FIG. 2. (a) HAS diffraction scans for Bi_2Se_3(111) measured at various incident energies with the sample at 113 K, aligned along the $\overline{\Gamma M}$ azimuth. The smaller features between the specular and the two diffraction peaks are due to bound-state resonances and kinematic focusing [51]. The vertical shaded regions next to the diffraction peaks illustrate additional features which appear to be independent of E_i, at a distance of about 0.2 Å^{-1} form the specular and first order diffraction peaks. (b) The temperature dependence of the Debye-Waller exponent of Bi_2Se_3(111) for the specular peak with the sample aligned along $\overline{\Gamma M}$.

III. RESULTS AND DISCUSSION

Figure 2(a) shows several diffraction scans along the $\overline{\Gamma M}$ azimuth plotted versus momentum transfer $\Delta K = |\Delta \mathbf{K}|$ parallel to the surface, while in Fig. 2(b), the temperature dependence of the specular peak intensity is plotted, which can be used to extract the e-ph coupling constant λ (Sec. III C). The diffraction scans in Fig. 2(a) have been measured at three different incident energies E_i, at a sample temperature of 113 K. The intensity scale has been scaled to show additional features with smaller intensity. Besides some features assigned to bound-state resonances and kinematic focusing, which are easily recognized due to the strong dependence of their position on the incident energy [30], there are features that occur at fixed values of ΔK, independently of E_i with a distance of about 0.2 Å^{-1} from the specular and first-order diffraction peaks, as indicated by the vertical shaded regions (further diffraction scans, including also the $\overline{\Gamma K}$ azimuth can be found in Appendix B).

We recently observed with HAS a multivalley charge density wave (CDW) in Sb(111) originating from the $\overline{M}$-point electron pockets giving rise to additional peaks in the diffraction pattern [52]. In Bi_2Se_3(111), however, no carrier pockets exist besides the Dirac cone and the quantum-well minibands occurring around the zone center [see Fig. 1(c)]. The latter provide nesting wave vectors of about 0.2 Å^{-1} between states of equal spin, which correspond fairly well to the parallel momentum transfers of the satellites observed aside the $(0, \pm 1)$ peaks in HAS diffraction spectra (and likely also aside the specular peak, despite the coincidence with bound-state resonances) [Fig. 2(a)]. Charge density structures typically show a strong temperature-dependent behavior and vanish when the temperature approaches T_c. In the present work, we performed full angular scans at 113 K and room temperature (see Fig. 10 in Appendix B). In comparison, the satellite peaks become smaller at room temperature but are still discernible above the inelastic background. While we do not have a full temperature-dependent measurement at hand which would allow a determination of, e.g., the critical exponent, it appears from the comparison that any transition temperature would be above room temperature, as we did not go to much higher temperatures due to the low melting point of the material and the risk of degrading the sample at those temperatures.

It should be noted, however, that the observation of satellite peaks whose position is independent of the HAS incident energy is by itself indicative of a long-period superstructure of the electron density, possibly incommensurate or weakly

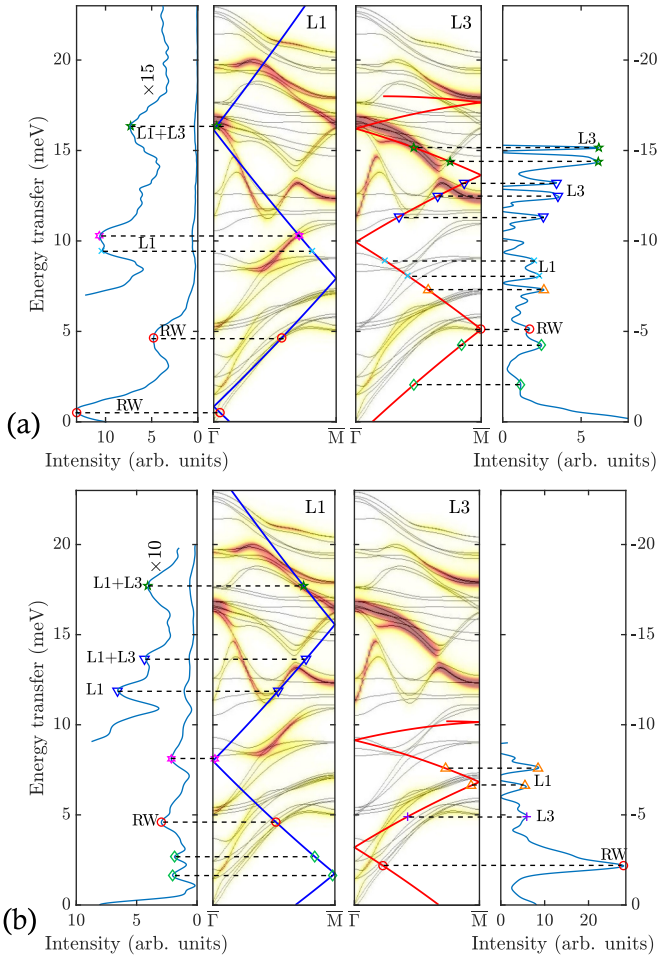

FIG. 3. Plot of two typical TOF measurements with the sample along $\overline{\Gamma M}$ and at room temperature. In (a), the incident energy is $E_i = 17.97$ meV with $\vartheta_i = 34.25°$ while in (b) $E_i = 10.19$ meV and $\vartheta_i = 40.25°$. The left and right-most panels show the TOF spectrum after conversion to energy transfer. The blue (phonon annihilation, $\Delta E > 0$) and red (phonon creation, $\Delta E < 0$) lines in the center panels show the scan curves superimposed onto the calculated dispersion using DFPT (The color code giving the intensity of the longitudinal L1 and L3 modes projected onto the first and third surface layer, respectively, is that of Fig. 5). The symbols denote peaks in the TOF spectrum which have been assigned to phonon events (RW = Rayleigh wave). The two distinct low-energy peaks (green diamonds) observed on the creation (a) and annihilation (b) sides in the phonon gap below the RW are tentatively assigned to low-energy collective surface electronic excitations, associated with the long-period surface superstructure and revealed through HAS bound-state resonance enhancement.

commensurate with the surface atomic lattice. Charge density oscillations as low as 10^{-6} atomic units, presently accessible to HAS, can in principle sustain very low-energy collective phase and amplitude excitations in the meV spectral range [52], and suggest an assignment of the present low-energy branches (Sec. III B).

A. Time-of-flight measurements and phonon dispersion curves

The phonon energies were determined by performing TOF measurements over a wide range of incident angles between

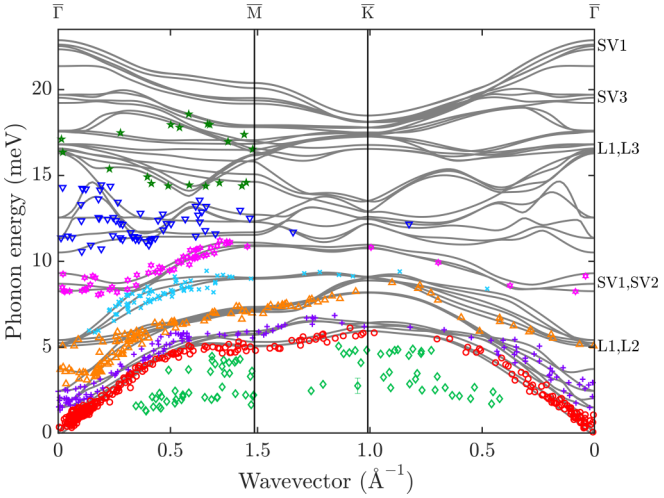

FIG. 4. Comparison of the measured phonon dispersion relation with DFPT calculations for three quintuple layers. The solid grey lines represent the DFPT calculation while different symbols for the experimentally determined points correspond to different phonon modes. The assignment of the symbols is based on the proximity to particular modes.

the first-order diffraction peaks and at various beam energies. The phonon dispersion was then obtained by calculating the parallel momentum transfer ΔK for each extracted phonon energy from the conservation laws of energy and parallel momentum providing the so-called scan curve for planar scattering (see Eq. (C1) in Appendix C and Refs. [23,53]).

In Fig. 3(a), an example of a TOF spectrum after conversion to the energy transfer scale is shown. The measurement was taken in the high-symmetry direction $\overline{\Gamma M}$ with an incident beam energy $E_i = 17.97$ meV and at an incident angle of $\vartheta_i = 34.25°$. The TOF spectrum consists of several peaks which are located on the creation ($\Delta E < 0$) as well as the annihilation ($\Delta E > 0$) side. The peak at zero energy transfer corresponds to elastically scattered helium atoms [28,29]. The scan curve, shown in the two center panels of Fig. 3 for phonon annihilation (blue) and creation (red) events, associates each phonon event with a specific momentum transfer ΔK. The scan curve has been backfolded into the irreducible part of the Brillouin zone and is plotted on top of the calculated dispersion. The different symbols on the scan curves, marking the main inelastic features, have been associated to phonons of different character and polarization.

The large peaks in the TOF spectra marked with the red circles in Fig. 3, correspond to the Rayleigh wave (RW) as seen in the DFPT calculations. Note that in the present TOF spectra, the RW exhibits typically the largest intensity of all inelastic events [cf. the intensities in Fig. 3(a)]. There is a fair correspondence between the present HAS data and those previously reported by Zhu *et al.* [17]. Curiously Zhu *et al.* stated that the RW is not observed, whereas it appears in their plot, though with only a few data points, in reasonable agreement with the present one in the $\overline{\Gamma K}$ direction; it also occurs in the $\overline{\Gamma M}$ direction, once it is recognized that there is an avoided crossing, so that the RW at $\overline{M}$ is not the lowest mode. There is however an important difference with respect to Zhu *et al.* [17]: Present HAS data do not show any evidence

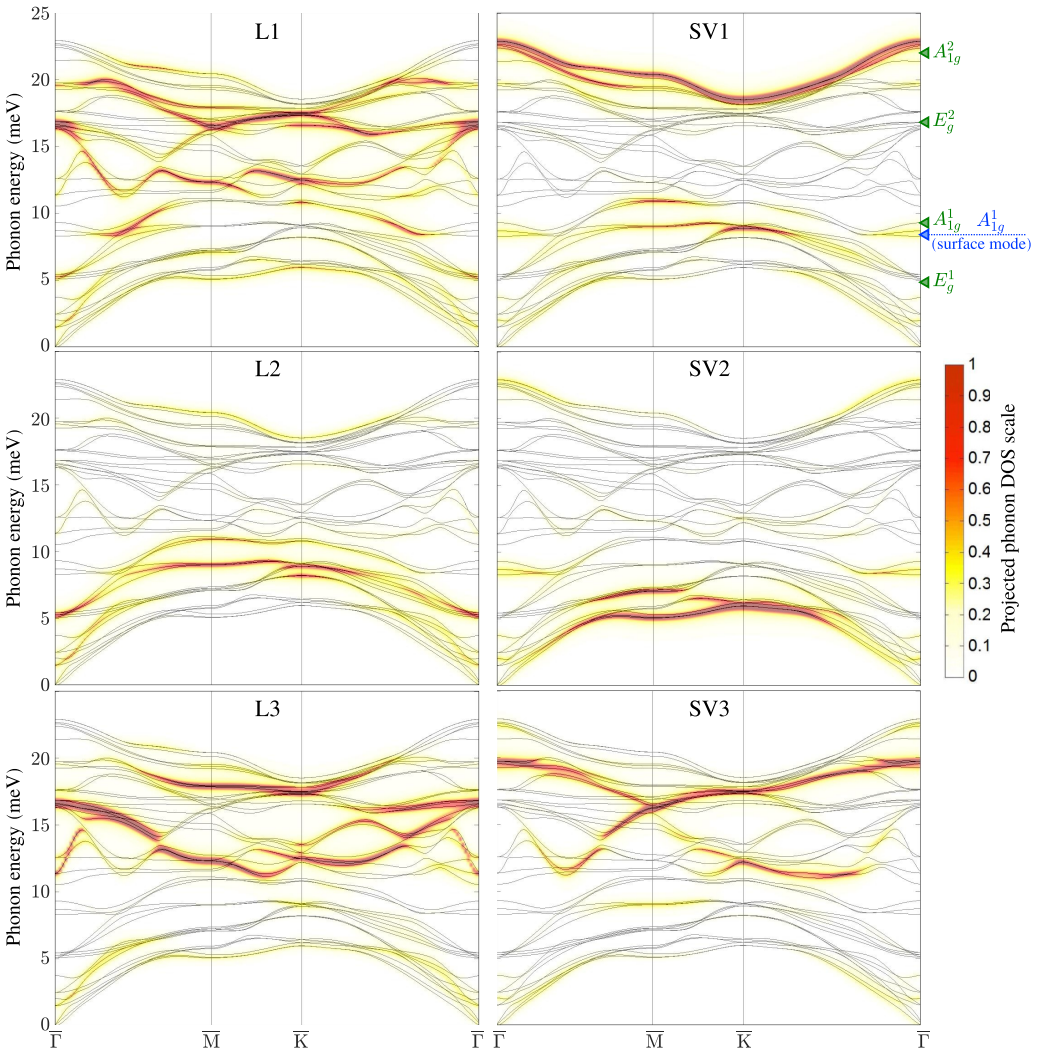

FIG. 5. Polarisation of the calculated phonon dispersion of Bi_2Se_3 from DFPT. The left column shows longitudinal polarization for the topmost three atomic layers (L1-L3). The right column shows shear vertical polarization (SV1-SV3). The color code bar on the right-hand side gives the intensity of the mode projected onto the corresponding layer. The green triangles at the top-right ordinate indicate the experimental energies of bulk Raman active modes according to Ref. [54], while the blue triangle shows the surface phonon softening according to Ref. [55].

of a KA in the ≈ 8 meV branch for wave vectors around 0.2 $Å^{-1}$ (see also Fig. 12 in Appendix C) and associated with the nesting at the Fermi level across the Dirac cone (or more likely across the parabolic dispersion of surface quantum-well states [19,20]).

Figure 4 shows the entire experimental surface phonon dispersion (symbols) superimposed onto the DFPT calculations (grey lines). The different symbols have been associated to phonons of different character and polarization based on the proximity to particular modes of the DFPT calculations. In total, we are able to distinguish at least eight different branches.

The polarization analysis of the calculated surface phonon modes can be found in Fig. 5 where the intensity of each polarization projected onto the corresponding layer is given by the color code. The left column shows the longitudinal polarisations for the first (L1), second (L2), and third (L3) layers. The right column shows the shear vertical polarization for the first three layers (SV1–SV3), while the shear horizontal polarization can be found in Fig. 9 of Appendix A. The theoretical dispersion curves are seen to agree quite well with the HAS data and also with the experimental Raman-active modes at $\overline{\Gamma}$ (green triangles in Fig. 5 according to [54]).

A closer comparison of the experimental data points in Fig. 4 with Fig. 5 shows that mainly phonon events with the largest amplitude in the two topmost layers of the sample are observed in the experiment. In particular in the low-energy region ($<$10 meV), most contributions come from phonons with the largest amplitude in the second layer (L2, SV2), which is a Bi layer and therefore about 2.5 times heavier than the first Se layer. The most prominent mode in the TOF spectra, the RW, corresponds predominantly to L and SV polarisations, due to its elliptical polarization, with a particularly strong SV2 component at the Brillouin zone boundary.

Note that the calculation does not reproduce the KA reported by Zhu *et al.* [17] (see Appendix A for calculations with SOC), in agreement with other recent *ab initio* calculations including SOC by Heid *et al.* [18] as well as with the

experimental and theoretical studies of $Bi_2Te_3(111)$ [28]. Heid *et al.* [18] suggested that the KA observed by Zhu *et al.* [7,17] may be connected to a strong e-ph interaction in the doped bulk material rather than to a surface state. According to their calculations, the largest contribution to the e-ph coupling comes from an in-plane polar-type branch in the optical region between 10 and 18 meV [18].

In fact, the strong dispersion of the optical phonon modes (Fig. 5), also found in Bi and Sb tellurides [28,50] may already be regarded as a manifestation of a significant e-ph interaction. In addition, Sobota *et al.* [55] reported a strong coupling of the A_{1g}^1 mode at a phonon energy of 8.48 meV which manifests itself in time-dependent renormalisations of the Dirac cone in angle-resolved photoemission spectroscopy (ARPES) measurements. The excellent quality of the DFPT calculations is further confirmed upon comparison with the experimentally observed softening of the A_{1g}^1 phonon mode at the surface, as reported by Sobota *et al.* [55] and as shown by the blue triangle in Fig. 5: The softening becomes apparent for the two lower branches of the DFPT calculations for three QLs.

We note that in the region around 15 meV the number of experimental data points is small and any mode assignment is probably accompanied by a large uncertainty, due to the strong dispersion and the avoided crossings of the calculated curves. Nevertheless it appears from the DFPT calculations that the optical phonon branch starting at about 16.5 meV at the $\overline{\Gamma}$ point softens to about 11 meV along $\overline{\Gamma M}$, in particular when considering the strong longitudinal character of this mode on the first atomic layer as shown in the top-left panel of Fig. 5. Such a softening could be caused by a screening of the quantum well electrons in analogy to the electron screening manifest as phonon softening of the optical phonon mode at 8.48 meV in the work of Sobota *et al.* [55], although in the latter case coupling appears mainly to the electrons of the Dirac cone rather than the quantum well states. It is also in accordance with our findings about the e-ph coupling (Sec. III C) which appears to be larger in the presence of a 2DEG upon comparison with systems that exhibit exclusively the Dirac topological states [27].

We turn now to the acoustic energy region and in particular the group velocity of the RW. In the long wavelength limit (close to $\overline{\Gamma}$) the dispersion relation of the RW is linear. Its slope provides the RW group velocity in the two symmetry directions $\overline{\Gamma M}$ and $\overline{\Gamma K}$:

$$\overline{\Gamma M}: v_{\mathrm{RW}}(112) = (1.63 \pm 0.07)\ \mathrm{km/s},$$
$$\overline{\Gamma K}: v_{\mathrm{RW}}(110) = (1.80 \pm 0.15)\ \mathrm{km/s}\ .$$

In order to appreciate the degree of localisation of the RW in the two symmetry directions, these values are to be compared with the corresponding speeds of sound. The present DFPT values (compared with values in parentheses derived from the available elastic constants [56]) are

$$\begin{aligned} \overline{\Gamma M}: \quad & v_{T,SV} = 1.757\ (1.91)\ \mathrm{km/s}, \\ & v_{T,SH} = 2.290\ (2.24)\ \mathrm{km/s}, \\ \overline{\Gamma K}: \quad & v_{T,SV} = 3.227\ (2.93)\ \mathrm{km/s}, \\ & v_{T,SH} = 1.416\ (1.22)\ \mathrm{km/s}\ . \end{aligned}$$

It appears that the RW has a velocity in the $\overline{\Gamma M}$ direction smaller than both transverse bulk values and is therefore a localized surface wave, whereas in the $\overline{\Gamma K}$ direction it has a velocity larger than that of the SH transverse sound, and is therefore a pseudosurface wave [57,58]. Actually in the absence of mirror symmetry for the sagittal plane in this direction, the RW is a resonance. The fact may have suggested (see Zhu *et al.* [7,17]) that in $Bi_2Se_3(111)$ the RW is suppressed but the present comparison with the DFPT calculation confirms that the RW is actually observed in both directions, though as a resonance along $\overline{\Gamma K}$. Values for the bulk longitudinal ($v_L = 2.9$ km/s) and transverse ($v_T = 1.7$ km/s) group velocities of Bi_2Se_3 have also been reported in the framework of the isotropic elastic continuum theory [8,59]. In this approximation, the corresponding RW velocity, obtained by solving the cubic Rayleigh equation [60], would be $v_{\mathrm{RW}} = 1.56$ km/s in any direction.

B. Low-energy branches

The measured HAS-TOF spectra displayed in Fig. 3 show also distinct peaks yielding two branches of elementary excitations with an energy below the RW branch (green diamonds in Fig. 4). On the basis of present DFPT surface phonon dispersion curves, they cannot be attributed to any possible phonon branch of the ideal surface. HAS from conducting surfaces exclusively occurs through the interaction (mostly Pauli repulsion) with the surface electron density, and therefore also electronic excitations in the THz range can be observed by HAS, with a 0.5 meV resolution and sensitivity to charge density oscillations in the 10^{-6} atomic units range.

Actually the observed low-energy branches are reminiscent of those recently observed with HAS in Sb(111), which have been attributed to elementary excitations (phasons/amplitons) of a multivalley CDW [52]. The concomitant presence of a commensurate component associated with the $\overline{\mathrm{M}}$-point electron pockets at the Fermi level, and an incommensurate one due to the hole pockets along the $\overline{\Gamma M}$ direction, allows for collective excitations with a comparatively small gap at $Q = 0$. On the other hand no low-energy phason/ampliton modes have been detected with HAS for the perfectly commensurate multivalley CDW reported in the quasi-1D surface Bi(114) [61], discommensuration being a requisite for depinning and a vanishing/small gap at $\overline{\Gamma}$. $Bi_2Se_3(111)$ has no pocket states at the Fermi level, besides the rings around $\overline{\Gamma}$ of the surface topological Dirac and the quantum-well states [19,20]. The satellites near the HAS diffraction peaks [see Fig. 2(a)] suggest some long-period charge-density structures and possibly low-energy collective excitations. In order to detect the associated, seemingly small inelastic features in the TOF spectra, we rely on the bound-state resonance enhancement method (Ref. [32] and Chap. 10 of Ref. [24]), applicable to highly corrugated surfaces and successfully used to detect with HAS high-energy optical surface modes in ionic crystals [24,62]. The complete set of He-surface bound states has been measured previously [51].

Bound-state inelastic resonances occur in the HAS-TOF spectrum, with a possibly large enhancement of the inelastic intensities, at the locus of intersections of the scan curve (1) [23] with the inelastic bound-state resonance condition (2)

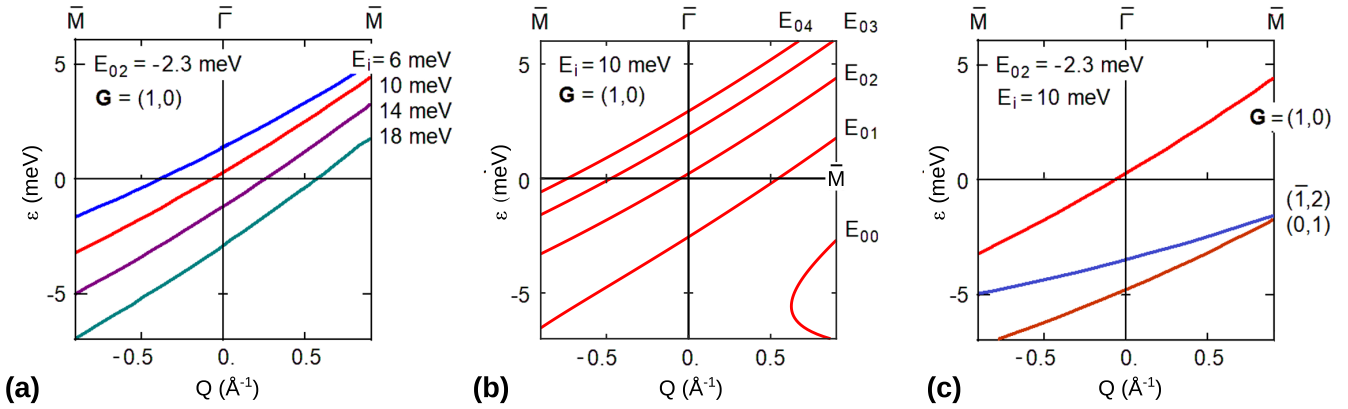

FIG. 6. Inelastic bound-state resonance conditions along the $\overline{\Gamma M}$ direction in the first Brillouin zone: (a) for $\mathbf{G} = (1, 0) \equiv (1.76, 0)$ Å^{-1}, the bound state $n = 2$ and different incident energies; (b) for a given $E_i = 10$ meV, $\mathbf{G} = (1,0)$ and the different bound states $n = 0, 1, \ldots, 4$; (c) for $E_i = 10$ meV, the bound state $n = 2$ and three different $\mathbf{G}$ vectors $(1, 0)$, $(\bar{1}, 2) \equiv (0, 3.05)$ Å^{-1}, $(0, 1) \equiv (0.88, 1, 53)$ Å^{-1}. Here, the integer indices refer to the hexagonal reciprocal lattice base, while the components in Å^{-1} units are those of $\mathbf{G} = (G_\parallel, G_\perp)$. Other $\mathbf{G}$-values yield inelastic resonances in the low-energy range $|\varepsilon| < 5$ meV only for wave vectors Q outside the first BZ. Suitable combinations of E_i, E_{0n}, and of the $\mathbf{G}$-vector permit to scan the phonon gap region below the RW branch, which can be used to tune the conditions for localized excitations, to detect those via a resonance enhancement.

(see Chap. 30 of Ref. [24]). For elementary excitations with an energy $\Delta E = \varepsilon$ and wave vector $\Delta K = Q$ the equations become

$$k_i \sin\vartheta_i + Q = \sin\vartheta_f \sqrt{2m(E_i + \varepsilon)/\hbar}, \tag{1}$$

$$E_i + \varepsilon = -|E_{0n}| + \frac{\hbar^2}{2m}\left[(k_i \sin\vartheta_i + Q + G_\parallel)^2 + G_\perp^2\right]. \tag{2}$$

At the mentioned intersection of (1) and (2), an elementary excitation with (ε, Q) assists the selective adsorption of the atom of mass m, incident energy E_i, wave vector k_i, and angle ϑ_i into a bound state of energy $-|E_{0n}|$, via the exchange of a surface reciprocal lattice vector $\mathbf{G} = (G_\parallel, G_\perp)$. On returning the $\mathbf{G}$ vector to the surface lattice, the atom is selectively desorbed from the bound state into the final angle ϑ_f. In (2), the vector $\mathbf{G}$ has been conveniently expressed via its components parallel and orthogonal to the scattering plane, respectively. In $Bi_2Se_3(111)$, the measured He-surface bound-state energies [51] are $E_{0n} = -5.6, -3.8, -2.3, -1.2, -0.5$ meV for $n = 0$, 1, 2, 3, 4, respectively. For a fixed scattering geometry $\vartheta_i + \vartheta_f = \vartheta_{SD}$ (here $\vartheta_{SD} = 91.5°$), Eqs. (1) and (2) provide, via the elimination of $\vartheta_i = \vartheta_{SD} - \vartheta_f$, the locus of intersections $\varepsilon = \varepsilon_{E_i,n;\mathbf{G}}(Q)$ for any incident energy E_i, bound state n and reciprocal surface vector $\mathbf{G}$.

The three panels of Fig. 6 show some plots of $\varepsilon = \varepsilon_{E_i,n;\mathbf{G}}(Q)$ in the $\overline{\Gamma M}$ direction for: (a) different values of the incident energy E_i at a given bound state ($n = 2$) and $\mathbf{G} = (1, 0)$; (b) different bound state energies at a given incident energy $E_i = 10$ meV; (c) several different $\mathbf{G}$ vectors at a given incident energy $E_i = 10$ meV and for the bound state $n = 2$. The functions $\varepsilon = \varepsilon_{E_i,n;\mathbf{G}}(Q)$ cross the phonon gap below the RW in the first BZ. In practice the phonon gap can be fully scanned by the resonance curves $\varepsilon = \varepsilon_{E_i,n;\mathbf{G}}(Q)$ upon varying the incident energy, so as to detect, via resonance enhancement, weak elementary excitations.

Since the low-energy data points appear to align along two dispersion curves, independently of the incident energy, as well as of n and $\mathbf{G}$, rather than being spread over the entire gap, they cannot be attributed to a resonance-enhanced many-phonon background. Furthermore, frustrated translational modes of adsorbates like CO would show no dispersion and would appear at higher vibrational energies [63]. More likely these points indicate two branches of low-energy excitations associated with the surface charge-density superstructure observed in the diffraction spectra, as anticipated above.

In this respect, it is worth mentioning a recent work by Shvonski *et al.* [36] where it is argued that a strong e-ph interaction affecting the surface 2DEG of a 3D topological crystal allows for collective polaron excitations (plasmon-polarons). Their dispersion is predicted to be that of an acoustic plasmon running below the single-particle excitation spectrum as an effect of the polaron-polaron attractive interaction. The theoretical analysis by Shvonski *et al.* [36] is actually interpreting the recent observation with high-resolution electron energy loss spectroscopy (HREELS) by Jia *et al.* [33] of an anomalous acoustic plasmon (AAP) mode from the topologically protected states of $Bi_2Se_3(111)$, with energy between 0 and 6.5 meV (and its continuation in the second zone up to ≈10 meV). The present HAS data do not permit to identify this AAP due to its superposition with the RW in the first BZ and in part with other phonon branches in its continuation.

C. Electron-phonon coupling

As shown in recent papers [25–27], the temperature dependence of the Debye-Waller (DW) exponent plotted in Fig. 2(b) permits to extract for a conducting surface the mass-enhancement parameter λ expressing the electron-phonon coupling strength. It is related to the DW exponent by the equations:

$$\lambda = \frac{\pi}{2n_s}\alpha\,, \quad \alpha \equiv \frac{\phi}{A_c\, k_{iz}^2}\frac{\partial \ln I(T_S)}{k_B\, \partial T_S}\,, \tag{3}$$

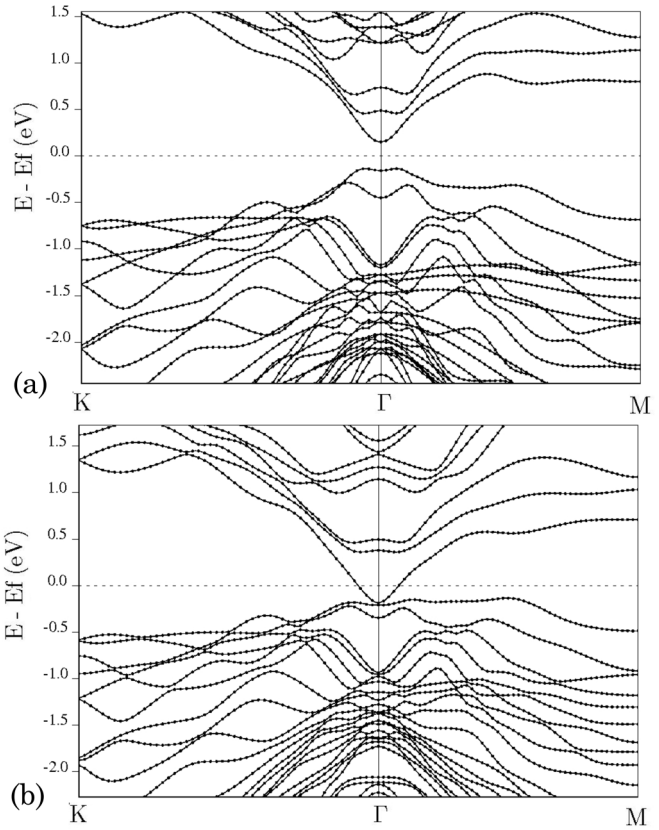

FIG. 7. Surface electronic band structure of Bi_2Se_3(111) omitting SOC (a). The topological surface states appear when SOC is included as shown in (b).

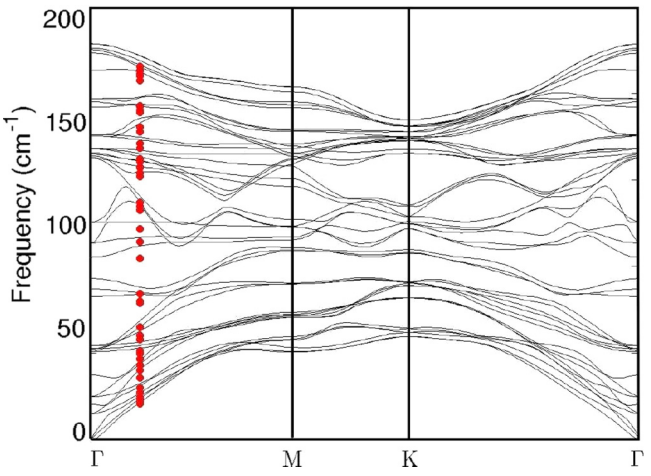

FIG. 8. Surface phonon dispersion of Bi_2Se_3 omitting (black continuous line) and including SOC (red dots) at a Q vector corresponding to the nesting vector $2k_F$. The inclusion of SOC gives rise to a softening of the phonon modes but no evidence for a KA is found.

where $\phi = 4.9$ eV is the work function [64], $A_c = 14.92$ Å^2 the unit cell area, $I(T_S)$ the He-beam specular intensity, T_S the surface temperature, $k_{iz} = 3.18$ Å^{-1} the normal component of the incident wave vector, and n_s the number of conducting layers which contribute to the phonon-induced modulation of the surface charge density.[1] The latter is estimated to be $n_s = 2\lambda_{TF}/c_0$, where λ_{TF} is the Thomas-Fermi screening length characterising the surface band-bending region (here ≈6 nm) [19], $c_0 = 9.6$ Å the QL thickness, and the factor 2 indicates the 2DEG multiplicity as observed with ARPES in the current Bi_2Se_3 sample [19]. With these values and the experimental DW derivative with respect to T_S from Fig. 2(b), we obtain $\lambda = 0.51$.

We note that there appear to be weak oscillations in the temperature-dependent data of Fig. 2(b). While deviations from a linear behavior could occur due to anharmonic effects at higher temperatures, or due to phonon-phonon coupling events, it appears from the experimental uncertainties that a linear regression provides still an accurate approximation in the present case. It should also be mentioned that, unlike in the case of low-index metal surfaces, characterized by a soft-wall repulsive potential and negligible corrugation, here the large electronic corrugation [51] implies a hard-wall potential. In this case, one needs to correct k_{iz}^2 so as to account for the acceleration impressed by the attractive part of the potential on the He atom when approaching the surface turning point (Beeby correction [29]). Therefore k_{iz}^2 is replaced by $k_{iz}'^2 = k_{iz}^2 + 2mD/\hbar^2$, where m is the He mass and $D = 6.54$ meV the He-surface potential well depth [51]. With the Beeby correction it is found $\lambda = 0.23$.

The value compares quite well with values in the literature derived from other experiments, e.g., $\lambda = 0.25$ [3], and $\lambda = 0.17$ [5] from ARPES measurements and $\lambda = 0.26$ [65] from Landau level spectroscopy. A theoretical study by Giraud *et al.* [8] with phonons calculated in the isotropic continuum limit gives $\lambda = 0.42$, whereas for other ARPES measurements, where only Dirac states appear to be involved, values of λ as low as 0.076 to 0.088 have been found [4].

From the comparison, it appears that the presence of a 2DEG due to quantum-well minibands (at least two in the present analysis) plays an important role in raising the e-ph coupling strength, which is quite small when exclusively due to the Dirac topological states, to values in the range of 0.2–0.4. It seems to be a general phenomenon for TIs belonging to the class of bismuth chalcogenides as reported by Benedek *et al.* [27]. The same conclusion follows from the theoretical analysis by Heid *et al.* [18], who showed that raising the Fermi level from the Dirac point to above the conduction band minimum gives a corresponding increase of λ from values well below 0.1 to values in the range above 0.2, with a substantial contribution from interband coupling and in very good agreement with the present analysis. The role of n-type doping contributing to the formation of the surface quantum-well 2DEG is quite clear in the analysis of the e-ph coupling strength in Cu-doped Bi_2Se_3, where an analysis

[1]The (bulk) carrier concentration as extracted from Hall measurements of the current sample is in the region (1.75–1.8) × 10^{18} cm^{-3}, i.e., a particularly small conductivity in the bulk suggesting that the carrier concentration at the surface may even be larger, compared to the first generation samples [19] which had a much larger bulk charge carrier concentration.

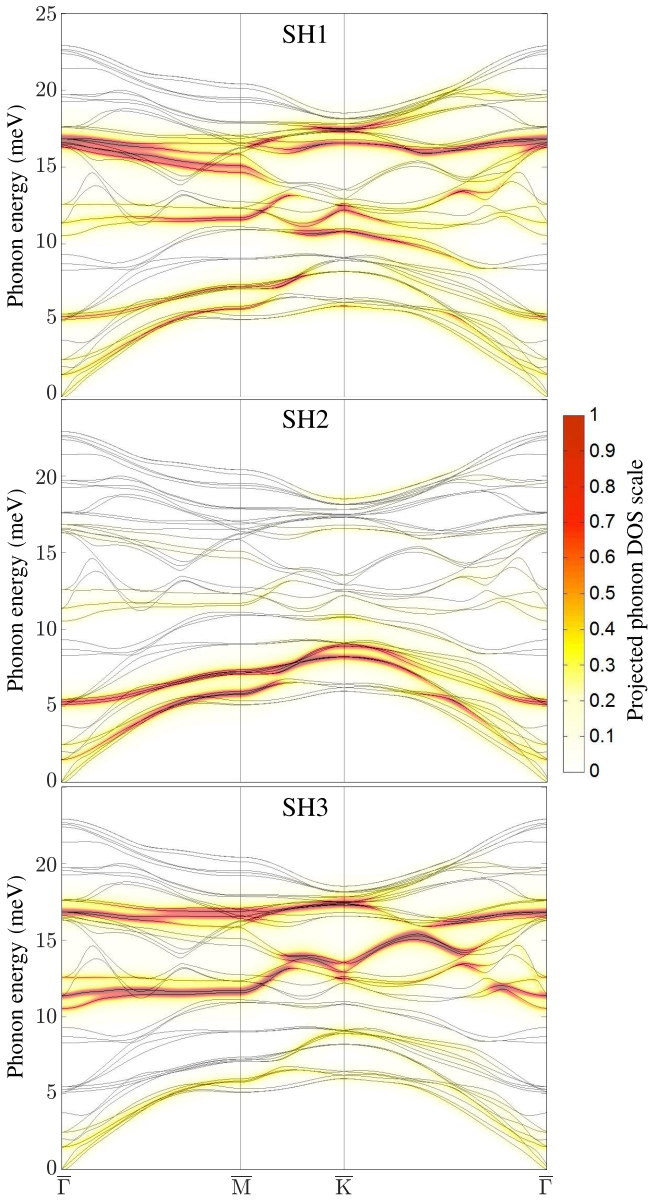

FIG. 9. Shear horizontal (SH) polarization of the calculated phonon dispersion of Bi_2Se_3 for the topmost three atomic layers (SH1-SH3) from DFPT without SOC. The color code bar on the right-hand side gives the intensity of the mode projected onto the corresponding layer.

based on the McMillan formula [66], indicates a value for λ as large as 0.62 [4].

IV. CONCLUSIONS

In summary, we have determined the surface phonon dispersion curves of Bi_2Se_3 along both high-symmetry directions, where the largest inelastic scattering intensity is provided by the Rayleigh wave. Thus our measurements show in contrast to previous studies that the Rayleigh mode exists and is a localized surface mode in one of the high-symmetry directions ($\overline{\Gamma M}$), while in the other high-symmetry direction it is actually a pseudo-surface wave ($\overline{\Gamma K}$). Comparison with density functional perturbation theory calculations shows

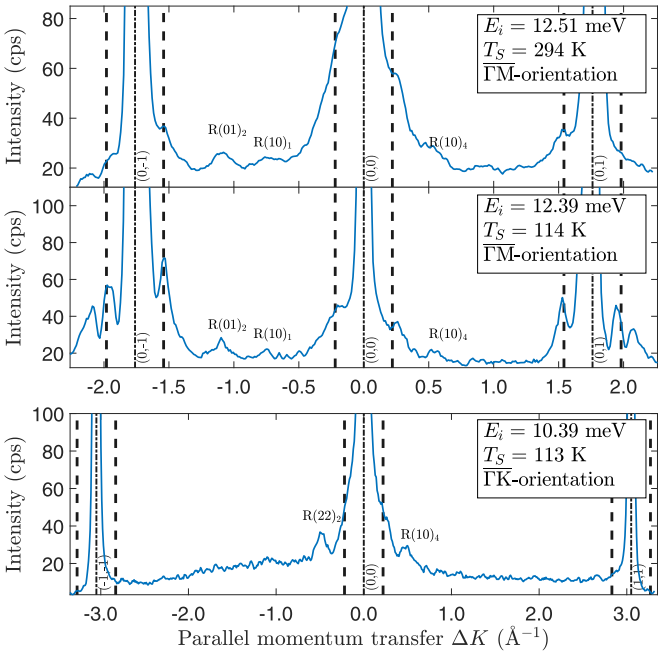

FIG. 10. HAS diffraction scans for Bi_2Se_3(111) measured at room temperature and 113 K along the high-symmetry direction $\overline{\Gamma M}$ and at low temperature along $\overline{\Gamma K}$. The smaller features between the specular and the two diffraction peaks are due to bound-state resonances and kinematical focusing [51].

excellent agreement with the experimental data. In addition to the phonon-related losses, we observe two additional dispersion curves in the gap well below the Rayleigh mode. These two low-energy branches may correspond to collective low-energy excitations of surface electrons. The appearance of these collective electronic excitations in an unprecedentedly low-energy region is probably associated with a small surface charge density and an appreciable electron-phonon coupling ($\lambda = 0.23$). However, much more detailed experiments and theoretical analysis will be needed in order to fully understand these excitations; e.g., what is the influence of the carrier concentration upon doping and what is the role of both the Dirac and the quantum-well states, with the latter providing a much larger electron-phonon interaction than the former. The analysis advocates for a more systematic study by means of elastic and inelastic HAS spectroscopy of the surface structure, the low-energy collective excitations, and the electron-phonon interaction of interesting 2D materials, where the superior space and energy resolution of HAS is hardly attainable with other current surface probes.

ACKNOWLEDGMENTS

We are grateful to Evgueni V. Chulkov (DIPC) and Krzysztof Kempa (Boston College) for useful discussions. The authors are grateful for financial support by the FWF (Austrian Science Fund) within the project P29641-N36 and A.T acknowledges financial support within the project J3479-N20. We would like to thank the Aarhus University Research Foundation, VILLUM FOUNDATION via the Centre of Excellence for Dirac Materials (Grant No. 11744) and the

SPP1666 of the DFG (Grant No. HO 5150/1-2) for financial support. M. Bremholm acknowledges financial support from the Center of Materials Crystallography (CMC) and the Danish National Research Foundation (DNRF93).

APPENDIX A: ADDITIONAL CALCULATIONS AND THE EFFECT OF SOC

Without SOC, Bi_2Se_3 exhibits a band gap, not only in the bulk but also at the surface with a band gap of 0.35 eV as evident from density functional theory (DFT) calculations [Fig. 7(a)]. By including SOC as shown in Fig. 7(b), the electronic band dispersion becomes gapless, with spin-polarized and Dirac cone shaped surface bands around the $\overline{\Gamma}$ point in the typical manner of 3D topological insulators.

The topologically protected Dirac cone forms a small Fermi circle around the $\overline{\Gamma}$ point which cannot be properly described with a coarse mesh and a large smearing resulting in the impossibility to capture subtle effects, such as the proposed KA [17] with a standard calculation. In order to verify the effect of such states on surface phonons, we repeated the phonon calculations at the Q point corresponding to the nesting vector ($2k_F$) by including SOC. We compared the result with that obtained by omitting the SOC.

To perform these calculations we had to improve the sampling of the Brillouin zone close to the Fermi surface which is particularly important to resolve a possibly existing anomaly. Given the peculiar shape of the Fermi surface in the Bi_2Se_3(111) slabs consisting of a ring around the $\overline{\Gamma}$ point, we used a graded k-point mesh (equivalent to a $50 \times 50 \times 1$ uniform mesh) near the $\overline{\Gamma}$ point and a coarser one (equivalent to a $8 \times 8 \times 1$ mesh) near the zone boundary. The results are reported in Fig. 8. A one to one comparison between phonon modes calculated with and without SOC shows that there is no evidence of a KA induced by the presence of the surface metallic states, involving any of the surface phonon modes. The spin-orbit coupling results merely in an overall softening of the phonon modes of at most 6%.

In addition to the shear vertical and shear horizontal phonon densities shown in the main part of the paper, Fig. 9 shows the shear horizontal polarisations projected onto the first, second and third layer (SH1, SH2, SH3). If the scattering plane, defined by the incoming and scattered He beam, coincides with a mirror plane of the surface, the detection of purely SH modes is, in principle, forbidden due to symmetry reasons [67] and we show the calculations of the SH modes here for completeness. However, phonon modes often exhibit a mixing of polarization components and even a purely SH mode may give rise to charge density oscillations above the first atomic layer which are eventually observed in inelastic He atom scattering.

APPENDIX B: ADDITIONAL DIFFRACTION SCANS

A comparison of two angular scans with 113 K and room temperature in the $\overline{\Gamma M}$ azimuth can be seen in Fig. 10. It shows that at higher temperatures the satellite peaks at constant momentum transfer are still present even though they are much smaller and sometimes appear as mere shoulders close to the diffraction peaks. In addition to the diffraction scans along $\overline{\Gamma M}$ which are already shown in the main part of the paper, Fig. 10 shows a diffraction scan along the $\overline{\Gamma K}$ azimuth.

Note that along $\overline{\Gamma K}$ there is no evidence for additional peaks close to the diffraction peaks, despite two small features close to the specular reflection which can be assigned to resonances [51]. The fact that these peaks appear only along $\overline{\Gamma M}$ is indicative of the hexagonal shape of the quantum well states giving rise to a multitude of connecting vectors with similar momentum transfer between the flat sides of the hexagon and thus along the $\overline{\Gamma M}$ azimuth.

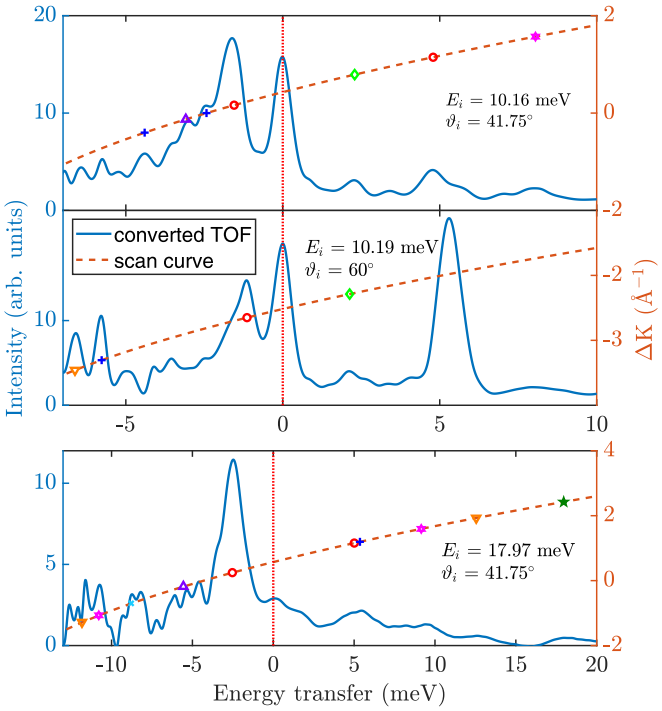

FIG. 11. Comparison of different TOF spectra in the $\overline{\Gamma M}$ direction with various incident Energies E_i and angles ϑ_i. For the two upper graphs the nozzle temperature was set to 50 K and for the bottom one to 80 K, while the sample was held at room temperature. The vertical red dotted line corresponds to elastically scattered atoms. The dashed line describes the scan curve which connects energy transfer with momentum transfer (y axis on the right-hand side). The symbols denote peaks in the TOF spectrum which have been assigned to phonon events (same symbols as the main part of the article).

APPENDIX C: FROM TOF MEASUREMENTS TO THE PHONON DISPERSION AND ADDITIONAL TOF DATA

The phonon energies were determined by performing TOF measurements over a wide range of incident angles between the first-order diffraction peaks and at various beam energies. The phonon dispersion was then obtained by calculating the parallel momentum transfer $\Delta K = |\Delta \mathbf{K}|$ for each extracted phonon energy ΔE from the conservation laws of energy and parallel momentum providing the so-called scan curve for

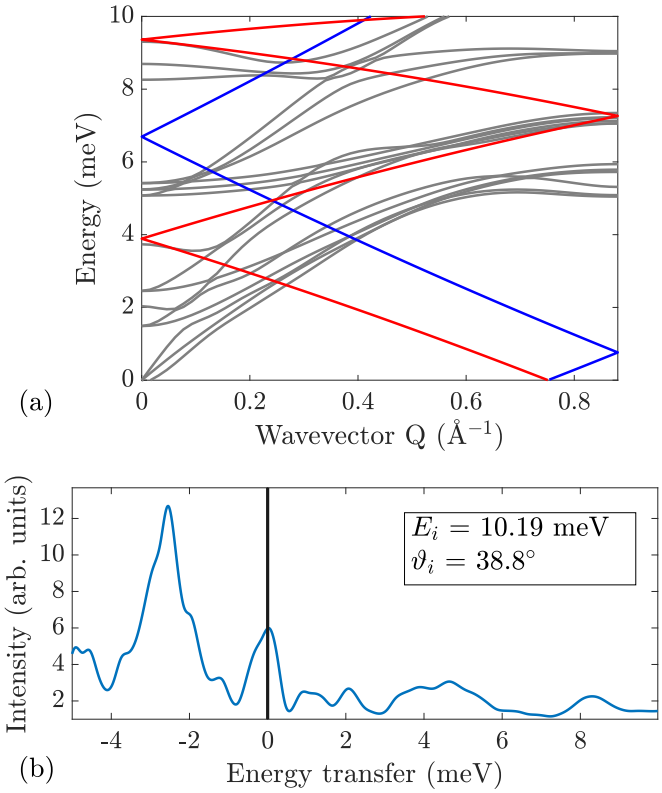

FIG. 12. In (b), the TOF spectrum with the x axis converted to energy transfer is shown. (a) depicts the corresponding scan curve [Eq. (C1)], backfolded into the first Brillouin zone and superimposed onto the results of the DFPT calculation (grey lines).

planar scattering [23,53]:

$$\frac{\Delta E}{E_i} + 1 = \frac{\sin^2 \vartheta_i}{\sin^2 \vartheta_f}\left(1 + \frac{\Delta \mathbf{K}}{\mathbf{K}_i}\right)^2, \tag{C1}$$

where E_i is the energy of the incident beam, $\mathbf{K}_i$ is the parallel component of the incident wave vector, and ϑ_i and ϑ_f are the incident and final angle, respectively.

Figures 11 and 12 show some further examples of measured TOF spectra along the $\overline{\Gamma M}$ azimuth and the sample at room temperature. Each TOF spectrum consists of various peaks which are located on the creation (negative x axis, $\Delta E < 0$) as well as the annihilation (positive x axis, $\Delta E > 0$) side. The peak at zero energy transfer corresponds to elastically scattered helium atoms due to the diffuse elastic peak which is caused by scattering from surface imperfections such as steps [28,29]. The scan curve associates each phonon event with a specific momentum transfer ΔK based on [Eq. (C1)], since the incoming helium atom looses or gains momentum via inelastic scattering from a phonon.

Figure 11 shows an additional set of TOF spectra along the $\overline{\Gamma M}$ direction. Most measurements covering the low-energy region with the acoustic phonon modes where performed with a ≈10 meV beam (top and center panel in Fig. 11), while for the optical phonon modes higher incident beam energies (bottom panel in Fig. 11) were used, in order to cover the optical energy region on the creation side. Note that the particularly strong peak at around 5.5 meV in the center panel is not assigned to a phonon event. This seemingly inelastic feature originates from elastic scattering and is caused by the outer tails of the velocity distribution in the incident beam. These so-called deceptons or spurions occur within the vicinity of the diffraction peaks and give rise to a large intensity in the inelastic spectra due to their elastic nature [68].

As mentioned in the main part of the article, there is no evidence for a strong KA in our measurements as reported by Zhu *et al.* [7,17], who observed a strong V-shaped indentation at $\Delta K \approx 0.25$ Å^{-1} for an optical phonon branch originating at 7.4 meV at the $\overline{\Gamma}$ point. The scan curve on the phonon annihilation side (blue curve) in Fig. 12(a) covers exactly the 6–8 meV close to the $\overline{\Gamma}$ point. Neither the DFPT calculations [grey lines in Fig. 12(a)] support such a KA nor does the experimental data which in turn even shows a minimum of the scattered inelastic intensity in the 6–8 meV region of the $\Delta E > 0$ side [Fig. 12(b)].

[1] M. Z. Hasan and C. L. Kane, Colloquium: Topological insulators, Rev. Mod. Phys. **82**, 3045 (2010).
[2] J. Moore, Topological insulators: The next generation, Nat. Phys. **5**, 378 (2009).
[3] R. C. Hatch, M. Bianchi, D. Guan, S. Bao, J. Mi, B. B. Iversen, L. Nilsson, L. Hornekær, and P. Hofmann, Stability of the Bi_2Se_3(111) topological state: Electron-phonon and electron-defect scattering, Phys. Rev. B **83**, 241303(R) (2011).
[4] Z.-H. Pan, A. V. Fedorov, D. Gardner, Y. S. Lee, S. Chu, and T. Valla, Measurement of an Exceptionally Weak Electron-Phonon Coupling on the Surface of the Topological Insulator Bi_2Se_3 Using Angle-Resolved Photoemission Spectroscopy, Phys. Rev. Lett. **108**, 187001 (2012).
[5] C. Chen, Z. Xie, Y. Feng, H. Yi, A. Liang, S. He, D. Mou, J. He, Y. Peng, X. Liu *et al.*, Tunable Dirac fermion dynamics in topological insulators, Sci. Rep. **3**, 2411 (2013).
[6] T. Kondo, Y. Nakashima, Y. Ota, Y. Ishida, W. Malaeb, K. Okazaki, S. Shin, M. Kriener, S. Sasaki, K. Segawa, and Y. Ando, Anomalous Dressing of Dirac Fermions in the Topological Surface State of Bi_2Se_3, Bi_2Te_3, and Cu-Doped Bi_2Se_3, Phys. Rev. Lett. **110**, 217601 (2013).
[7] X. Zhu, L. Santos, C. Howard, R. Sankar, F. C. Chou, C. Chamon, and M. El-Batanouny, Electron-Phonon Coupling on the Surface of the Topological Insulator Bi_2Se_3 Determined from Surface-Phonon Dispersion Measurements, Phys. Rev. Lett. **108**, 185501 (2012).
[8] S. Giraud, A. Kundu, and R. Egger, Electron-phonon scattering in topological insulator thin films, Phys. Rev. B **85**, 035441 (2012).
[9] P. Di Pietro, M. Ortolani, O. Limaj, A. Di Gaspare, V. Giliberti, F. Giorgianni, M. Brahlek, N. Bansal, N. Koirala, S. Oh, P. Calvani, and S. Lupi, Observation of Dirac plasmons in a topological insulator, Nat. Nanotechnol. **8**, 556 (2013).

[10] K. Kadel, L. Kumari, W. Li, J. Y. Huang, and P. P. Provencio, Synthesis and thermoelectric properties of Bi_2Se_3 nanostructures, Nanoscale Res. Lett. **6**, 57 (2011).

[11] S. K. Mishra, S. Satpathy, and O. Jepsen, Electronic structure and thermoelectric properties of bismuth telluride and bismuth selenide, J. Phys.: Condens. Matter **9**, 461 (1997).

[12] H. J. Goldsmid, *Thermoelectric Refrigeration* (Springer, 1964).

[13] J. Liang, L. Cheng, J. Zhang, H. Liu, and Z. Zhang, Maximizing the thermoelectric performance of topological insulator Bi_2Te_3 films in the few-quintuple layer regime, Nanoscale **8**, 8855 (2016).

[14] H. Tang, X. Wang, Y. Xiong, Y. Zhao, Y. Zhang, Y. Zhang, J. Yang, and D. Xu, Thermoelectric characterization of individual bismuth selenide topological insulator nanoribbons, Nanoscale **7**, 6683 (2015).

[15] A. J. Minnich, M. S. Dresselhaus, Z. F. Ren, and G. Chen, Bulk nanostructured thermoelectric materials: Current research and future prospects, Energy Environ. Sci **2**, 466 (2009).

[16] T.-C. Hsiung, C.-Y. Mou, T.-K. Lee, and Y.-Y. Chen, Surface-dominated transport and enhanced thermoelectric figure of merit in topological insulator $Bi_{1.5}Sb_{0.5}Te_{1.7}Se_{1.3}$, Nanoscale **7**, 518 (2015).

[17] X. Zhu, L. Santos, R. Sankar, S. Chikara, C. Howard, F. C. Chou, C. Chamon, and M. El-Batanouny, Interaction of Phonons and Dirac Fermions on the Surface of Bi_2Se_3: A Strong Kohn Anomaly, Phys. Rev. Lett. **107**, 186102 (2011).

[18] R. Heid, I. Y. Sklyadneva, and E. V. Chulkov, Electron-phonon coupling in topological surface states: The role of polar optical modes, Sci. Rep. **7**, 1095 (2017).

[19] M. Bianchi, D. Guan, S. Bao, J. Mi, B. B. Iversen, P. D. King, and P. Hofmann, Coexistence of the topological state and a two-dimensional electron gas on the surface of Bi_2Se_3, Nat. Commun. **1**, 128 (2010).

[20] P. D. C. King, R. C. Hatch, M. Bianchi, R. Ovsyannikov, C. Lupulescu, G. Landolt, B. Slomski, J. H. Dil, D. Guan, J. L. Mi, E. D. L. Rienks, J. Fink, A. Lindblad, S. Svensson, S. Bao, G. Balakrishnan, B. B. Iversen, J. Osterwalder, W. Eberhardt, F. Baumberger, and P. Hofmann, Large Tunable Rashba Spin Splitting of a Two-Dimensional Electron Gas in Bi_2Se_3, Phys. Rev. Lett. **107**, 096802 (2011).

[21] G. Grimvall, *The Electron-Phonon Interaction in Metals* (North-Holland, Amsterdam, 1981).

[22] I. Y. Sklyadneva, G. Benedek, E. V. Chulkov, P. M. Echenique, R. Heid, K.-P. Bohnen, and J. P. Toennies, Mode-Selected Electron-Phonon Coupling in Superconducting Pb Nanofilms Determined from He Atom Scattering, Phys. Rev. Lett. **107**, 095502 (2011).

[23] A. Tamtögl, P. Kraus, M. Mayrhofer-Reinhartshuber, D. Campi, M. Bernasconi, G. Benedek, and W. E. Ernst, Surface and subsurface phonons of Bi(111) measured with helium atom scattering, Phys. Rev. B **87**, 035410 (2013).

[24] G. Benedek and J. P. Toennies, *Atomic Scale Dynamics at Surfaces* (Springer, Berlin, Heidelberg, 2018).

[25] G. Benedek, S. Miret-Artés, J. P. Toennies, and J. R. Manson, Electron-phonon coupling constant of metallic overlayers from specular he atom scattering, J. Phys. Chem. Lett. **9**, 76 (2018).

[26] A. Tamtögl, P. Kraus, N. Avidor, M. Bremholm, E. M. J. Hedegaard, B. B. Iversen, M. Bianchi, P. Hofmann, J. Ellis, W. Allison, G. Benedek, and W. E. Ernst, Electron-phonon coupling and surface Debye temperature of Bi_2Te_3(111) from helium atom scattering, Phys. Rev. B **95**, 195401 (2017).

[27] G. Benedek, S. Miret-Artés, J. R. Manson, A. Ruckhofer, W. E. Ernst, and A. Tamtögl, Origin of the electron-phonon interaction of topological semimetal surfaces measured with helium atom scattering, J. Phys. Chem. Lett. **11**, 1927 (2020).

[28] A. Tamtögl, D. Campi, M. Bremholm, E. M. J. Hedegaard, B. B. Iversen, M. Bianchi, P. Hofmann, N. Marzari, G. Benedek, J. Ellis, and W. Allison, Nanoscale surface dynamics of Bi_2Te_3(111): Observation of a prominent surface acoustic wave and the role of van der Waals interactions, Nanoscale **10**, 14627 (2018).

[29] D. Farías and K.-H. Rieder, Atomic beam diffraction from solid surfaces, Rep. Prog. Phys. **61**, 1575 (1998).

[30] M. Mayrhofer-Reinhartshuber, P. Kraus, A. Tamtögl, S. Miret-Artés, and W. E. Ernst, Helium-surface interaction potential of Sb(111) from scattering experiments and close-coupling calculations, Phys. Rev. B **88**, 205425 (2013).

[31] V. M. Silkin, A. García-Lekue, J. M. Pitarke, E. V. Chulkov, E. Zaremba, and P. M. Echenique, Novel low-energy collective excitation at metal surfaces, Europhys. Lett. **66**, 260 (2004).

[32] D. Evans, V. Celli, G. Benedek, J. P. Toennies, and R. B. Doak, Resonance-Enhanced Atom Scattering from Surface Phonons, Phys. Rev. Lett. **50**, 1854 (1983).

[33] X. Jia, S. Zhang, R. Sankar, F.-C. Chou, W. Wang, K. Kempa, E. W. Plummer, J. Zhang, X. Zhu, and J. Guo, Anomalous Acoustic Plasmon Mode from Topologically Protected States, Phys. Rev. Lett. **119**, 136805 (2017).

[34] F. Stern, Polarizability of a Two-Dimensional Electron Gas, Phys. Rev. Lett. **18**, 546 (1967).

[35] T. Ando, A. B. Fowler, and F. Stern, Electronic properties of two-dimensional systems, Rev. Mod. Phys. **54**, 437 (1982).

[36] A. Shvonski, J. Kong, and K. Kempa, Plasmon-polaron of the topological metallic surface states, Phys. Rev. B **99**, 125148 (2019).

[37] H. Yu and J. C. Hermanson, Subband structure and plasmon-phonon coupled excitations in the accumulation layer of ZnO, Phys. Rev. B **41**, 5991 (1990).

[38] J. M. Pitarke, V. M. Silkin, E. V. Chulkov, and P. M. Echenique, Theory of surface plasmons and surface-plasmon polaritons, Rep. Prog. Phys. **70**, 1 (2006).

[39] Y. Wang, E. W. Plummer, and K. Kempa, Foundations of plasmonics, Adv. Phys. **60**, 799 (2011).

[40] B. Diaconescu, K. Pohl, L. Vattuone, L. Savio, P. Hofmann, V. M. Silkin, J. M. Pitarke, E. V. Chulkov, P. M. Echenique, D. Farías, and M. Rocca, Low-energy acoustic plasmons at metal surfaces, Nature (London) **448**, 57 (2007).

[41] A. Tamtögl, M. Sacchi, N. Avidor, I. Calvo-Almazán, P. S. M. Townsend, M. Bremholm, P. Hofmann, J. Ellis, and W. Allison, Nanoscopic diffusion of water on a topological insulator, Nat. Commun. **11**, 278 (2020).

[42] A. Tamtögl, M. Mayrhofer-Reinhartshuber, N. Balak, W. E. Ernst, and K. H. Rieder, Elastic and Inelastic Scattering of He Atoms from Bi(111), J. Phys.: Condens. Matter **22**, 304019 (2010).

[43] M. Michiardi, I. Aguilera, M. Bianchi, V. E. de Carvalho, L. O. Ladeira, N. G. Teixeira, E. A. Soares, C. Friedrich, S. Blügel, and P. Hofmann, Bulk band structure of Bi_2Te_3, Phys. Rev. B **90**, 075105 (2014).

[44] X. Chen, H. D. Zhou, A. Kiswandhi, I. Miotkowski, Y. P. Chen, P. A. Sharma, A. L. L. Sharma, M. A. Hekmaty, D. Smirnov, and Z. Jiang, Thermal expansion coefficients of Bi_2Se_3 and Sb_2Te_3 crystals from 10 K to 270 K, Appl. Phys. Lett. **99**, 261912 (2011).

[45] A. Tamtögl, E. A. Carter, D. J. Ward, N. Avidor, P. R. Kole, A. P. Jardine, J. Ellis, and W. Allison, Note: A simple sample transfer alignment for ultra-high vacuum systems, Rev. Sci. Instrum. **87**, 066108 (2016).

[46] S. Baroni, S. de Gironcoli, A. Dal Corso, and P. Giannozzi, Phonons and related crystal properties from density-functional perturbation theory, Rev. Mod. Phys. **73**, 515 (2001).

[47] P. Giannozzi, S. Baroni, N. Bonini, M. Calandra, R. Car, C. Cavazzoni, D. Ceresoli, G. L. Chiarotti, M. Cococcioni, I. Dabo, A. D. Corso, S. de Gironcoli, S. Fabris, G. Fratesi, R. Gebauer, U. Gerstmann, C. Gougoussis, A. Kokalj, M. Lazzeri, L. Martin-Samos, N. Marzari, F. Mauri, R. Mazzarello, S. Paolini, A. Pasquarello, L. Paulatto, C. Sbraccia, S. Scandolo, G. Sclauzero, A. P. Seitsonen, A. Smogunov, P. Umari, and R. M. Wentzcovitch, QUANTUM ESPRESSO: A modular and open-source software project for quantum simulations of materials, J. Phys.: Condens. Matter **21**, 395502 (2009).

[48] J. P. Perdew, K. Burke, and M. Ernzerhof, Generalized Gradient Approximation Made Simple, Phys. Rev. Lett. **77**, 3865 (1996).

[49] M. Alcántara Ortigoza, I. Y. Sklyadneva, R. Heid, E. V. Chulkov, T. S. Rahman, K.-P. Bohnen, and P. M. Echenique, *Ab initio* lattice dynamics and electron-phonon coupling of Bi(111), Phys. Rev. B **90**, 195438 (2014).

[50] D. Campi, M. Bernasconi, and G. Benedek, *Ab-initio* calculation of surface phonons at the Sb_2Te_3(111) surface, Surf. Sci. **678**, 46 (2018).

[51] A. Ruckhofer, A. Tamtögl, M. Pusterhofer, M. Bremholm, and W. E. Ernst, Helium-surface interaction and electronic corrugation of Bi_2Se_3(111), J. Phys. Chem. C **123**, 17829 (2019).

[52] A. Tamtögl, P. Kraus, M. Mayrhofer-Reinhartshuber, G. Benedek, M. Bernasconi, D. Dragoni, D. Campi, and W. E. Ernst, Statics and dynamics of multivalley charge density waves in Sb(111), npj Quantum Mater. **4**, 28 (2019).

[53] S. A. Safron, High-resolution helium atom scattering as a probe of surface vibrations, Adv. Chem. Phys. **95**, 129 (1996).

[54] I. Boulares, G. Shi, E. Kioupakis, P. Lošt'ák, C. Uher, and R. Merlin, Surface phonons in the topological insulators Bi_2Se_3 and Bi_2Te_3, Solid State Commun. **271**, 1 (2018).

[55] J. A. Sobota, S.-L. Yang, D. Leuenberger, A. F. Kemper, J. G. Analytis, I. R. Fisher, P. S. Kirchmann, T. P. Devereaux, and Z.-X. Shen, Distinguishing Bulk and Surface Electron-Phonon Coupling in the Topological Insulator Bi_2Se_3 Using Time-Resolved Photoemission Spectroscopy, Phys. Rev. Lett. **113**, 157401 (2014).

[56] X. Gao, M. Zhou, Y. Cheng, and G. Ji, First-principles study of structural, elastic, electronic and thermodynamic properties of topological insulator Bi_2Se_3 under pressure, Philos. Mag. **96**, 208 (2016).

[57] G. W. Farnell, Properties of elastic surface waves, in *Physical Acoustics*, Vol. 6, edited by W. P. Mason and R. N. Thurston (Academic Press, 1970), Vol. 6, pp. 109–166.

[58] G. W. Farnell, Types and properties of surface waves, in *Acoustic Surface Waves*, edited by A. A. Oliner, Topics in Applied Physics Vol. 24 (Springer-Verlag, Berlin, Heidelberg, 1978), pp. 13–60.

[59] Y. D. Glinka, S. Babakiray, T. A. Johnson, M. B. Holcomb, and D. Lederman, Acoustic phonon dynamics in thin-films of the topological insulator Bi_2Se_3, J. Appl. Phys. **117**, 165703 (2015).

[60] A. A. Maradudin and G. I. Stegeman, Surface acoustic waves, in *Surface Phonons*, edited by F. W. W. Kress (Springer, Heidelberg, 1991), pp. 5–35.

[61] P. Hofmann, M. M. Ugeda, A. Tamtögl, A. Ruckhofer, W. E. Ernst, G. Benedek, A. J. Martínez-Galera, A. Stróżecka, J. M. Gómez-Rodríguez, E. Rienks, M. F. Jensen, J. I. Pascual, and J. W. Wells, Strong-coupling charge density wave in a one-dimensional topological metal, Phys. Rev. B **99**, 035438 (2019).

[62] G. Bracco, R. Tatarek, S. Terreni, and F. Tommasini, Surface optical phonons in LiF(001) observed by inelastic helium scattering, Phys. Rev. B **34**, 9045 (1986).

[63] A. P. Graham, The low energy dynamics of adsorbates on metal surfaces investigated with helium atom scattering, Surf. Sci. Rep. **49**, 115 (2003).

[64] J. Suh, D. Fu, X. Liu, J. K. Furdyna, K. M. Yu, W. Walukiewicz, and J. Wu, Fermi-level stabilization in the topological insulators Bi_2Se_3 and Bi_2Te_3: Origin of the surface electron gas, Phys. Rev. B **89**, 115307 (2014).

[65] I. Zeljkovic, K. L. Scipioni, D. Walkup, Y. Okada, W. Zhou, R. Sankar, G. Chang, Y. J. Wang, H. Lin, A. Bansil, F. Chou, Z. Wang, and V. Madhavan, Nanoscale determination of the mass enhancement factor in the lightly doped bulk insulator lead selenide, Nat. Commun. **6**, 6559 (2015).

[66] W. L. McMillan, Transition temperature of strong-coupled superconductors, Phys. Rev. **167**, 331 (1968).

[67] A. Tamtögl, E. Bahn, J. Zhu, P. Fouquet, J. Ellis, and W. Allison, Graphene on Ni(111): Electronic corrugation and dynamics from helium atom scattering, J. Phys. Chem. C **119**, 25983 (2015).

[68] W. Allison, R. F. Willis, and M. Cardillo, Origin of the anomalous low-frequency losses observed in the inelastic scattering of He atoms from LiF(001), Phys. Rev. B **23**, 6824 (1981).